Nanoscale

PAPER

View Article Online
View Journal | View Issue

Check for updates

Cite this: *Nanoscale*, 2025, **17**, 8634

# Effect of channel patterning precision on the performances of vertical OECTs†

Ruhua Wu,[a] Chufeng Wu,[a] Jinhao Zhou,[a] Liang-Wen Feng,[b] Jianhua Chen,[c] Dan Zhao*[a] and Wei Huang*[a]

Received 12th December 2024,
Accepted 5th March 2025

DOI: 10.1039/d4nr05239k

rsc.li/nanoscale

Precise patterning of electronic functional layers is vital for integrated electronics, where high integration density is required. Similarly, for organic electrochemical transistors (OECTs), the patterning precision of the channel layer is essential for device miniaturization, parasitic capacitance reduction, and accurate performance evaluation. In particular, for an emerging OECT architecture, vertical OECT (vOECT), the effect of patterning precision on key device parameters (such as transconductance ($g_m$) and transient time ($\tau$)) remains unclear. Here, controllable patterning of vOECT channel regions is realized by direct laser etching, where 2–100 μm margin lengths ($l_M$) are left beyond the vertical channel area. By quantitatively analyzing the impact of margin areas on device performance (including drain currents ($I_D$), $g_m$, and $\tau$), it has been found that a larger $l_M$ leads to significantly increased $I_D$ and $g_m$ in both n- and p-type OECTs (106.94% and 61.46% enhancement of $I_D$ and 102.92% and 92.59% enhancement of $g_m$ in n- and p-type OECTs, respectively, are observed as $l_M$ increases), which saturate under an $l_M$ of ~60 μm. Nevertheless, linearly increasing $\tau$ (from hundreds of microseconds to a few milliseconds) is observed with increasing $l_M$, revealing that parasitic capacitance outside the channel would result in a longer redox reaction time but not always higher $I_D$ and $g_m$. It is revealed that the patterning precision of active layers alters the OECT performances tremendously and can be designed to meet different application requirements (either high amplification capability, high integrating density, or fast response time) in OECT-based electronics.

Published on 07 March 2025. Downloaded on 3/15/2026 4:49:12 AM.

## Introduction

Organic electrochemical transistors (OECTs), consisting of organic mixed ionic–electronic conductor (OMIEC)-based channels, exhibit mixed ionic and electronic coupling and transport capabilities.[1–3] Therefore, exceptionally high transconductances ($g_m$, >10 mS) can be acquired in OECTs due to large volumetric capacitance (>10 F cm$^{-3}$) by ion doping into the channel, making them ideal for biosensors with simultaneous sensing and amplification capabilities.[4–6] Moreover, OECTs can be further integrated into complementary logic circuits with good biocompatibility and biomimetic properties,[7–11] which can be further applied in next-generation neuromorphic electronics and brain–computer interfaces.[12–15] The performances of OECTs can be improved through various methods, including polymer backbone design and side-chain engineering,[16–18] gate/electrolyte or channel/electrolyte interface optimization,[19–21] and device structural innovation.[22–24]

In particular, by introducing a vertical device geometry, vertical OECTs (vOECTs), which are distinct from the conventional planar OECTs (cOECTs), demonstrated a reduced channel length (OMIEC film thickness) of less than ~100 nm, an enhanced $g_m$ of 0.2–0.4 S, an on/off current ratio ($I_{on}/I_{off}$) of ~10$^7$, a transient time ($\tau$) of less than 1 ms, and ultra-high cycling stability (>50 000 cycles).[22,25,26] Such high transistor performances rely on a transistor channel with photopatterning capability by mixing OMIECs with photo crosslinkers. Moreover, precise and well-defined OMIEC patterning not only facilitates device integration, enhances integration density, and reduces crosstalk, but also significantly impacts the performances of individual devices, including $g_m$, $I_{on}/I_{off}$, *etc.*[27–29] For instance, Enrico *et al.*[30] demonstrated that by using femtosecond laser microfabrication to pattern the encapsulation and OMIEC layers of cOECTs, a significantly shortened $\tau$ (from hundreds of milliseconds to hundreds of microseconds) was achieved. Moreover, research on the patterning of semiconductor layers in planar thin-film transistors (TFTs) has shown that precise patterning of the active region would con-

[a]*School of Automation Engineering, University of Electronic Science and Technology of China (UESTC), 611731 Chengdu, China. E-mail: danzhao@uestc.edu.cn, whuang@uestc.edu.cn*
[b]*Key Laboratory of Green Chemistry & Technology, Ministry of Education, College of Chemistry, Sichuan University, Chengdu, 610065, China*
[c]*Department of Chemical Science and Technology, Yunnan University, Kunming, China*

† Electronic supplementary information (ESI) available. See DOI: https://doi.org/10.1039/d4nr05239k


This journal is © The Royal Society of Chemistry 2025

Published on 07 March 2025. Downloaded on 3/15/2026 4:49:12 AM.

tribute to better transient performances.[31,32] Even though a previous study revealed that the contact area in planar OECTs would also affect the transistor dynamic characteristics,[32] for vOECTs, studies that provide a quantitative analysis of the impact of patterning precision on the performance metrics are still missing. Providing such a correlation between device performance and channel patterning precision would be extremely valuable to guide the design, fabrication, and optimization of vOECT-based electronics.

Here, vOECTs based on n-type poly(benzimidazobenzophenanthroline) (BBL) and p-type poly(2,5-dipentaethyleneglycol-3,6-di(thiophen-2-yl)-2,5-dihydropyrrolo[3,4-*c*]pyrrole-1,4-dione-*alt*-2,5-bis(3-triethyleneglycoloxythiophen-2-yl)) (gDPP-g2T) as the channel OMIECs (Fig. S1†) are fabricated and characterized to examine the effects of channel patterning precision on the transistor's static and dynamic performances. A picosecond direct laser writing (DLW) system is applied to precisely pattern the BBL-based channel, achieving a patterning resolution and alignment accuracy of <2 μm. Consequently, by increasing the margin length ($l_M$) of the OMIEC pattern from 2 μm to 100 μm for BBL-based vOECTs (Fig. 1), $I_{on}$ and $I_{off}$ increase from 0.36 ± 0.01 mA and 0.75 ± 0.11 nA to 0.72 ± 0.86 mA and 4.81 ± 0.97 nA, respectively. Meanwhile, $\tau_{on}$ (turn-on transient time) and $\tau_{off}$ (turn-off transient time) grow from 2.16 ± 0.11 and 0.43 ± 0.07 ms to 7.64 ± 0.93 and 1.60 ± 0.17 ms, respectively, as $l_M$ increases from 2 to 100 μm. Similar trends on these key parameters are also observed in p-type gDPP-g2T-based vOECTs. Specifically, $I_{on}$ increases with the expanded $l_M$ and reaches a plateau, which can be well-fitted by employing a fringing effect model, while $I_{off}$ is dominated by the channel capacitance, following a quadratic function concerning $l_M$. On the other hand, $\tau$ exhibits an approximately linear trend depending on $l_M$, which agrees with that in the Bernards model.[33] This work indicates that a larger margin region beyond the effective channel area contributes to additional $I_{on}$ and $g_m$ due to parasitic currents, but slower device response due to larger volume capacitance. Consequently, a quantitative relationship between vOECT performance and channel patterning precision is established, which provides guidelines for the optimal demand-oriented design of bioelectronics with either high amplification capability (high $g_m$), fast response (short $\tau$), or dense integration.

**Wei Huang**

*Wei Huang obtained his B.S. in physics from Nankai University and his Ph.D. in optical engineering from the University of Electronic Science and Technology of China (UESTC). He was a research assistant professor at Northwestern University, under the supervision of Professor Tobin J. Marks and Professor Antonio Facchetti. Currently, he is a Professor at the School of Automation Engineering, UESTC. His research interests include flexible/stretchable electronics, neuromorphic electronics, and transistor-based chemical/biological sensors.*

## Results and discussion

n-Type vOECTs were fabricated on 1 mm thick glass substrates by vertically stacking a bottom Au electrode, a DLW-patterned BBL film, a top Au electrode, and an encapsulation layer (Fig. 1a). The detailed fabrication process can be found in the Experimental section, where vOECTs with approximately 100 nm thick BBL (Fig. S2 and Table S1†) sandwiched between top (drain) and bottom (source) electrodes with the same electrode width ($W_T$ and $W_B$) of 30 μm were fabricated. In particular, the OMIEC films were patterned within different $l_M$ of 2, 5, 10, 20, 40, 60, 80, and 100 μm, respectively, beyond the overlapping effective channel region, where the encapsulation layer has the same opening size as that of the patterned OMIEC film (Fig. 1b, c and S3†). The DLW process effectively ensures patterning and alignment precision between the bottom electrode and the semiconductor film within 2 μm.

The transfer, $g_m$, and subthreshold swing (SS) characteristics of the vOECTs based on BBL with varied $l_M$ are demonstrated in Fig. 2a–c, where $I_D$, gate current ($I_G$), and $g_m$ exhibit obvious increasing trends as $l_M$ expands. It should be noted that due to the geometric symmetry of the vOECT, selecting either the top or bottom electrode as the source or drain electrode would not significantly affect device performances (Fig. S4†). At the same time, the lowest SS remains relatively unchanged at approximately 65 mV dec$^{-1}$ in all devices. Meanwhile, the slightly negatively shifted threshold voltage ($V_{th}$) with increasing $l_M$ suggests that more ionic injection pathways towards the channel and/or smaller electrode–channel interface resistance with a larger margin area may be formed (Fig. S5†). Specifically, as shown in Fig. 2d, $I_{on}$ ($I_D$ under $V_G$ = 0.6 V and $V_D$ = 0.1 V) gradually increases from 0.36 ± 0.01, 0.47 ± 0.04, 0.51 ± 0.05, 0.62 ± 0.02 and 0.67 ± 0.03 mA with an $l_M$ of 2, 5, 10, 20, and 40 μm, respectively. Then, $I_{on}$ reaches a plateau of ~0.72 mA when $l_M$ is ≥60 μm. For $I_G$, as the $l_M$ increases from 2 μm to 100 μm, an approximately two orders of magnitude increase in $I_G$ (from ~$10^{-9}$ A to $10^{-7}$ A at $V_G$ = 0.6 V and from $10^{-10}$ A to $10^{-8}$ A at $V_G$ = −0.2 V) is observed. Such a phenomenon indicates that, as enlarged $l_M$ leads to more margin areas other than the direct channel area (the overlapping area of top and bottom electrodes), pronounced ion injection/extraction behavior in the OMIEC channel would result in extra electron carrier transport paths between source/drain electrodes.

Next, a fringe field effect model, which has already been validated for its effectiveness in planar thin film transistors,[34] is employed to fit the above $I_D$ variation. Here, the $I_D$ of

Published on 07 March 2025. Downloaded on 3/15/2026 4:49:12 AM.

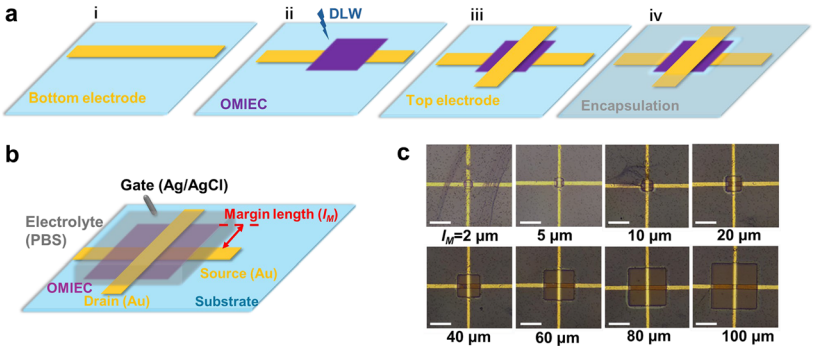


**Fig. 1** (a) Fabrication flow diagrams of a DLW patterned vOECT, (i) bottom electrode deposition and patterning, (ii) OMIEC channel spin-coating and patterning, (iii) top electrode deposition, and (iv) encapsulation layer deposition and patterning. (b) Schematic of a vOECT and definition of the margin length ($l_M$). (c) Microscopy images of the BBL-based vOECTs with different patterning precisions (scale bar = 100 μm).

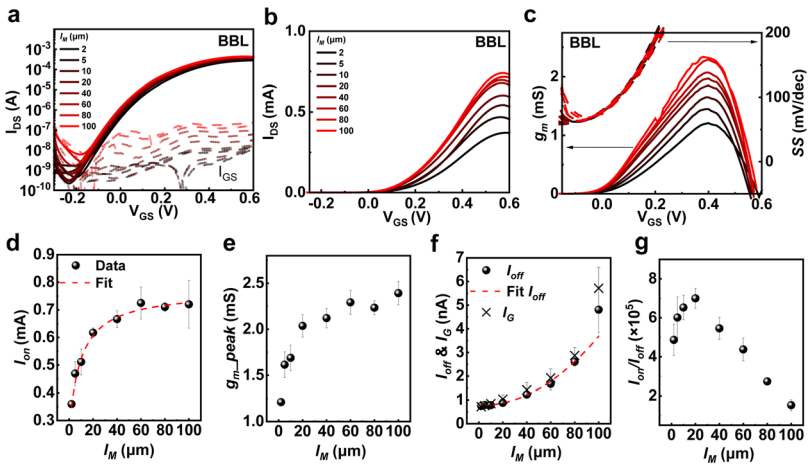


**Fig. 2** (a–c) Transfer characteristics ($V_D$ = 0.1 V) on the log scale (a) and linear scale (forward scan only) (b), and plots of $g_m$ and SS of BBL-based vOECTs with varied $l_M$. (d–g) Key parameters of $I_{on}$ (d), $g_m$ (e), $I_{off}$ along with $I_G$ in the off-state (f), and the on/off ratio (g) of BBL-vOECTs as a function of $l_M$ (error bars represent the standard deviation of 5 individual vOECTs from 3 batches).

vOECTs can be divided into two components, expressed by the following formula:

$$I_D = I_{ch} + I_{fr} \tag{1}$$

where $I_{ch}$ is the portion of current contributed by the direct channel area demonstrated by Bernards' model[33] and $I_{fr}$ is the parasitic current generated by the fringe field in the redundant area. Meanwhile, current flux ($J$) can then be expressed as eqn (2) according to Ohm's law:

$$J = q\mu n(\boldsymbol{r})E(\boldsymbol{r}) \tag{2}$$

where $q$ is the elementary charge, $\mu$ is the carrier mobility, $n$ is the electron density, $E$ is the electric field, and $\boldsymbol{r}$ is the position vector. A schematic of a vOECT with a redundant pattern at the electrode edge is shown in Fig. S6.† It is assumed that in the quasi-2D OMIEC thin film, the electric field is distributed along the $z$-direction, while the field and concentration dependence is neglected, meaning that both $n$ and $\mu$ are set to be constants.[33,35] Therefore, $I_{fr}$ can be expressed as follows:

$$I_{fr} = q\mu n \int E_{fr}(S)\mathrm{d}S \tag{3}$$

where $E_{fr}$ is the fringing field. Since providing precise numerical calculations of the fringing electric field is highly challenging, we approximate the distribution of $E_{fr}$ within the redundant semiconductor regions using Lumerical Charge simulations (see the ESI note†). The simulation results (Fig. S7†) reveal that $E_{fr}$ exhibits decay proportional to $x^{-2}$ and depends on the potential difference between the top and bottom electrodes and the distance between the electrodes ($d$, OMIEC film thickness):

$$E_{fr}(x) = \frac{V_D A}{d} x^{-2} \tag{4}$$

where $A$ is an area factor. Considering only the regions where the OMIEC film is in direct contact with the electrodes (areas ①, ② and ③, ④ in Fig. S6†), the expression for $I_{fr}$ can be derived as follows:

 This journal is © The Royal Society of Chemistry 2025

Published on 07 March 2025. Downloaded on 3/15/2026 4:49:12 AM.

$$I_{fr} = q\mu n \cdot 2(W_B + W_T)\frac{V_D A}{d}\int x^{-2}\mathrm{d}x \quad (5)$$

where $W_B$ and $W_T$ are the bottom and top electrode widths, respectively. Thus, the parasitic current within $l_M$ from 2 μm (the highest patterning precision) to $x$ μm ($x$ > 2 μm) can be obtained by evaluating the integral of eqn (5) over the range [2, $x$]:

$$I_{fr} = q\mu n \cdot 2(W_B + W_T)\frac{V_D A}{d}\left(\frac{1}{2} - \frac{1}{x}\right) \quad (6)$$

Consequently, the data in Fig. 2d are fitted by combining eqn (1) and (6). It should be noted that this model only considers the OMIEC margin areas that make direct contact with the electrodes (areas ①–④, Fig. S6†) while disregarding the areas that are not making direct contact with the electrodes (areas ⑤–⑧, Fig. S6†). As shown in Fig. 2d, under such a model, a good fitting result is demonstrated with excellent agreement on the measured $I_{on}$. Furthermore, Fig. 2e illustrates peak $g_m$ of vOECTs with varied $l_M$ of 2, 5, 10, 20, 40, 60, 80, and 100 μm being 1.21 ± 0.03, 1.62 ± 0.14, 1.70 ± 0.14, 2.04 ± 0.12, 2.12 ± 0.11, 2.29 ± 0.13, 2.23 ± 0.08, and 2.39 ± 0.12 mS, respectively. The $g_m$ variation concerning $l_M$ corresponds to that of $I_{on}$, exhibiting sharp growth followed by a plateauing trend. This suggests that the parasitic current effect in the redundant OMIEC region predominantly contributes to this portion of $g_m$.

Compared to $I_{on}$, the increase in the $I_{off}$ of vOECTs is more apparent, which rises from 0.75 ± 0.11 nA to 4.81 ± 0.97 nA as $l_M$ increases from 2 to 100 μm. According to the current discrete model, $I_D$ ($I_{off}$) is composed of two parts: $I_{CH}$ and $I_{GD}$.[36–38] In the off-state of vOECTs, $I_{CH}$ contributes little to $I_D$ due to the negligible conductivity of pristine BBL.[39] Thus, $I_{off}$ is dominated by the portion of $I_{GD}$ (Fig. S8†). Based on the variation in $I_G$ during the off-state of the OECT, it can be observed that they are proportional to the OMIEC redundant area between the electrolyte and the channel, exhibiting a quadratic relationship concerning $l_M$ (Fig. 2f). It is concluded that $I_G$ is primarily dominated by the volume capacitance of the channel, which is reflected by the ionic doping/dedoping currents.[28] Furthermore, the electrolyte–gold electrode contact has been demonstrated to affect the performance of the vOECT, particularly the $I_{off}$ (Fig. S9 and S10†). Therefore, accurate patterning of the OMIEC channel is beneficial for improved $I_{on}/I_{off}$ ratios (Fig. 2g). As the $l_M$ decreases from 100 μm to 20 μm, the $I_{on}/I_{off}$ ratio of the BBL-based vOECT increases from (1.53 ± 0.28) × $10^5$ to (7.00 ± 0.51) × $10^5$. It should be noted that further reducing $l_M$ causes an abnormal increase in $I_{on}/I_{off}$, which is due to possible short circuits between the top and bottom electrodes as shorter $l_M$ may lead to imperfect gapping between electrodes, resulting in a slight decrease in $I_{on}/I_{off}$ for more precisely patterned vOECTs ($l_M$ < 10 μm).

To validate the transistor performance variation trend affected by channel patterning precision, p-type gDPP-g2T-based vOECTs are also fabricated and characterized with different $l_M$. It should be noted that a photolithography patterning process is employed by mixing gDPP-g2T with a photocrosslinker (double-end trifluoromethyl diazirine (DtFDA)). Here, p-type thin films with a thickness of ~124 nm and an $l_M$ of 5 to 100 μm are fabricated (Fig. S2, S11–12 and Table S1†). The transfer characteristics of the p-type OECT are shown in Fig. 3a, where the SS and $V_{th}$ remain relatively constant with varying $l_M$, with values of 95.44 ± 1.08 mV $dec^{-1}$ and −0.30 ± 0.01 V, respectively (Fig. 3b and c). As $l_M$ increases from 5 μm to 100 μm, $I_{on}$ increases from 3.42 ± 0.11 to 5.67 ± 0.24 mA, which can be fitted using the fringe field model (Fig. 3d). Similarly, $g_m$ increases from 13.36 ± 0.49 mS to 20.08 ± 1.45 mS as $l_M$ increases from 5 μm to 100 μm (Fig. 3e), while $I_{off}$ increases from 12.76 ± 1.41 to 157.78 ± 20.08 nA, demonstrating a trend similar to that in n-type vOECTs, which fits well with a quadratic function of $l_M$, indicating proportionality to the patterned area (channel capacitance) (Fig. 3f). Furthermore, the effect of patterning on $I_{on}/I_{off}$ follows the

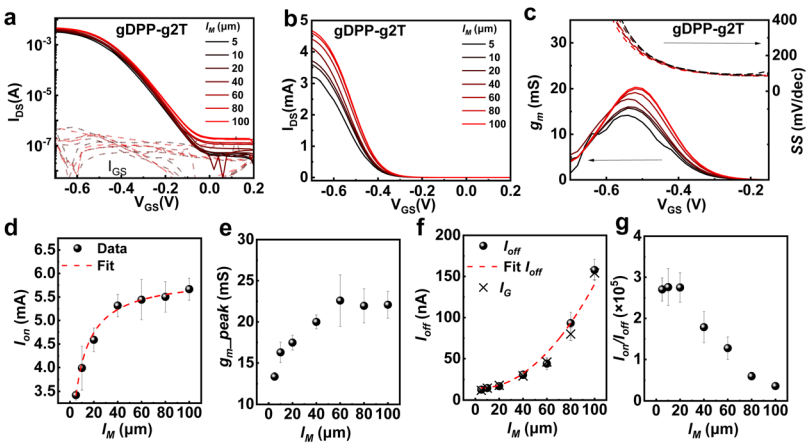


Fig. 3 (a–c) Transfer characteristics ($V_D$ = −0.1 V) on the log scale (a) and linear scale (forward scanning only) (b), and plots of $g_m$ and SS of vOECTs with a gDPP-g2T channel with varied $l_M$. (d–g) Key parameters of $I_{on}$ (d), $g_m$ (e), $I_{off}$ along with $I_G$ in the off-state (f), and the on/off ratio (g) of gDPP-g2T-vOECTs as a function of $l_M$ (error bars represent the standard deviation of 5 individual vOECTs from 3 batches).

Published on 07 March 2025. Downloaded on 3/15/2026 4:49:12 AM.

same trend as that observed in the n-type OECT. As $l_M$ increases from 5 μm to 100 μm, $I_{on}/I_{off}$ decreases from (2.70 ± 0.28) × $10^5$ to (0.36 ± 0.05) × $10^5$ (Fig. 3g). These results confirm the assumptions for n-type OECTs and indicate that the impact of semiconductor patterning on device performance is independent of the type of charge carrier.

Additionally, the impacts of patterned precision on the transient characteristics of the vOECTs are investigated. Fig. 4a shows the transient curves of the n-type vOECTs with $l_M$ varying from 2 μm to 100 μm. It should be noted that the applied input pulses ($V_{GS}$) exhibit a spike width of 0.1 s and an amplitude from −0.3 V to 0.5 V, along with a $V_{DS}$ of 0.1 V. The extracted $\tau$ are presented in Fig. 4b and c, where $\tau_{on}$ and $\tau_{off}$ increase from 2.16 ± 0.11 ms and 0.43 ± 0.07 ms to 7.64 ± 0.93 ms and 1.60 ± 0.17 ms, respectively, as $l_M$ increases from 2 μm to 100 μm. Both $\tau_{on}$ and $\tau_{off}$ exhibit an approximately linear relationship with $l_M$. According to the ionic circuit that describes the ionic transition in the electrolyte of OECTs, the $\tau$ of OECTs is related to the solution resistance ($R_S$) and channel capacitance ($C_{CH}$) (Fig. S13(i)†).[38] Imperfectly patterned regions of the BBL can generate parasitic capacitance ($C_{Pr}$), leading to variations in the transient response time of vOECTs. Considering the influence of $C_{Pr}$, the ionic circuit is transformed into Fig. S13(ii),† where $\tau \propto R_S'(C_{CH} + C_{Pr})$. From the electrochemical impedance spectroscopic (EIS) measurement (Fig. S14†) of the vOECTs, where the corresponding values of

$$R_S'(C_{CH} + C_{Pr})$$

are calculated, it exhibits an approximately linear variation concerning $l_M$ (Fig. S15†). Similarly, the transient characteristics of the p-type OECT are shown in Fig. 4d. By fitting the data, it is revealed that the variation of $\tau_{on}$ and $\tau_{off}$ for $l_M$ still shows obvious linear characteristics (Fig. 4e and f). Additionally, the cycling stabilities of BBL-based vOECTs with different patterning precisions are investigated (Fig. S16–18†). The results indicate that redundant semiconductor areas would not significantly affect $I_{on}$ and $g_m$ during the stability measurement. The $I_{on}$ of the devices with $l_M$ = 5, 40, and 100 μm decay to 86.67%, 89.01%, and 81.63% of their initial values after 50 000 cycles, while the values of $g_m$ are 89.42%, 88.76%, and 86.33%. However, the increase in $I_{off}$ is significantly more pronounced in the vOECT with $l_M$ = 5 μm compared to devices with larger patterns. This suggests that electrochemical reactions at the film edges may exacerbate structural variations in the polymer impairing the device's off-state performance.

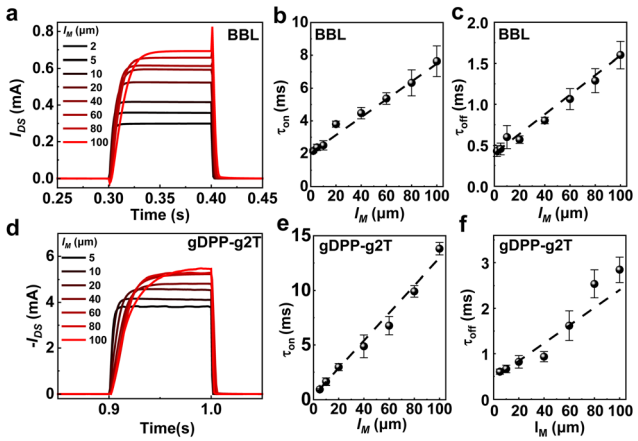


Fig. 4 Transient response (a) and the plots of $\tau_{on}$ (b) and $\tau_{off}$ (c) of n-type vOECTs as a function of $l_M$. Transient response (d) and the plots of $\tau_{on}$ (e) and $\tau_{off}$ (f) of p-type vOECTs as a function of $l_M$ (error bars represent the standard deviation of 5 individual vOECTs from 3 batches).

## Conclusions

In this work, the key performance metrics of both n- and p-type vOECTs, including $I_{on}$, $I_{off}$, $g_m$, $I_{on}/I_{off}$, and $\tau$ for patterning precision, have been investigated by adopting DLW for n-type OMIECs and photopatterning for p-type ones. It is revealed that the expansion of $l_M$ enhances the $I_{on}$ and $g_m$ of vOECTs but also leads to higher $I_{off}$ and longer $\tau$. As $l_M$ increases, $I_{on}$ and $g_m$ increase significantly and saturate with $l_M$ > 40 μm. A fringe field model considering parasitic currents from the OMIEC that makes direct contact with the source/drain electrode outside the channel area shows good fitting to experimental trends. Additionally, an increase is observed in $I_{off}$ and $I_G$, following a quadratic relationship with $l_M$, which is attributed to the additional margin areas that introduce higher channel capacitance and an additional leakage path. Moreover, channel patterning precision also influences the dynamic performance of vOECTs. As $l_M$ decreases, the $\tau_{on}$ and $\tau_{off}$ of both n-type and p-type vOECTs are significantly reduced. This improvement in $\tau$ with a shorter $l_M$ is due to the less parasitic capacitance. These findings underscore the importance of patterning precision in the vOECT channel and provide guidance and reference for optimizing the performance of organic electronics based on OECTs.

## Experimental section

### Materials

gDPP-g2T, DtFDA, and cinnamate-cellulose (Cin-Cell) were synthesized based on previous reports.[22,40–42] SU-8 and the SU-8 developer were purchased from Wenhao Co., Ltd. BBL, isopropyl alcohol and chloroform were purchased from Sigma-Aldrich. Phosphate buffer saline (PBS) is supplied by Solarbio and used as the aqueous electrolyte.

### Solution preparation

gDPP-g2T and Cin-Cell were first dissolved in chloroform with a concentration of 20 mg $mL^{-1}$, respectively. DtFDA was dissolved in chloroform with a concentration of 100 mg $mL^{-1}$. These solutions were stirred at room temperature overnight. Solutions for the p-type channel layers were prepared by mixing the solution gDPP-g2T with the solution of DtFDA and Cin-Cell to yield a weight ratio of 10 : 1 : 6. A blend solution of

 This journal is © The Royal Society of Chemistry 2025

Published on 07 March 2025. Downloaded on 3/15/2026 4:49:12 AM.

20 mg mL$^{-1}$ Cin-Cell and 100 mg mL$^{-1}$ DtFDA with a weight ratio of 4 : 1 was prepared for the precursor of the encapsulation layer. A solution for the n-type channel layers was prepared by solving BBL in methanesulfonic with a concentration of 20 mg mL$^{-1}$.

### vOECT fabrication

**n-Type vOECTs.** Glass substrates were first sonicated in soap water, deionized water, acetone, and isopropyl alcohol for 15 minutes, respectively, followed by UV-ozone cleaning (Shenzhen Hwo Technology Co., Ltd) for 15 min. Then, 3 nm Cr and 150 nm Au layers were thermally evaporated (in a vacuum at 1.5 × 10$^{-3}$ Pa, at deposition rates of ~0.1 Å s$^{-1}$ for Cr and ~1.5 Å s$^{-1}$ for Au, respectively), subsequently. Patterning of electrodes is next accomplished using a DLW system (R4, LPKF Laser & Electronics AG, Germany) with a laser power of 0.5 W and a frequency of 200 kHz, followed by an additional 15-minute sonication in isopropyl alcohol and UV-ozone treatment. Subsequently, 20 mg mL$^{-1}$ BBL solution was spin-coated at 3000 rpm for 1 min. Then, the BBL thin films were patterned within different $l_M$ by using the DLW system (a laser power of 0.11 W and a frequency of 500 kHz). Then, a 150 nm Au top electrode was thermally evaporated at a rate of ~1.5 Å s$^{-1}$ under vacuum (1.5 × 10$^{-3}$ Pa). Subsequently, for n-type OECTs, an SU-8 encapsulation layer was spin-coated at 2000 rpm for 1 min followed by a 1 min soft bake before cross-linking with 365 nm UV exposure for 20 s. Subsequently, after an additional 1 min of post-exposure bake, the encapsulation layer was developed in isopropyl alcohol and the developer.

**p-Type vOECTs.** Glass substrates were cleaned following the same processes as n-type vOECTs. Then, 3 nm Cr and 150 nm Au layers were thermally evaporated (in a vacuum at 1.5 × 10$^{-3}$ Pa, at deposition rates of ~0.1 Å s$^{-1}$ for Cr and ~1.5 Å s$^{-1}$ for Au, respectively) with a shadow mask, followed by an additional 15-minute UV-ozone treatment. Subsequently, p-type blending (gDPP-g2T : DtFDA : Cin-Cell = 10 : 1 : 6 in the weight ratio) was spin-coated at 3000 rpm for 30 s. The gDPP-g2T thin films were then cross-linked by exposure to 365 nm UV for 3 min and 285 nm UV for 2 min with a photomask, followed by developing in chloroform for ~3 s and blow drying. The 150 nm Au top electrode was thermally evaporated at a rate of ~1.5 Å s$^{-1}$ under vacuum (1.5 × 10$^{-3}$ Pa). Subsequently, the Cin-Cell : DtFDA encapsulation blend was spin-coated at 3000 rpm for 30 s in the glove box and cross-linked by 365 nm UV exposure for 2 min with a photomask and developed in chloroform for 3 s.

### vOECTs' electrical measurement

Electrical characterization was conducted with an FS-Pro semiconductor parameter analyzer along with a probe station (Chengdu Chiptest Technology Co., Ltd). An ~2 μL droplet of PBS (1×) solution was applied to the active area with the insertion of an Ag/AgCl gate electrode (World Precision Instruments, EP-1) in the electrolyte. For BBL-based vOECTs, the transfer curves were collected after the devices were cycled with transfer characteristics 6 times while for gDPP-g2T-based devices, no cycling was conducted before the acquisition of the transfer curves. Stability characterization was conducted by maintaining a consistent PBS electrolyte concentration (0.01 M) with a PDMS reservoir with a volume of approximately 0.5 × 0.5 × 0.5 cm$^3$ on the top of the device's active area and approximately 50 mL electrolyte added. The Ag/AgCl electrode was immersed in the electrolyte to act as the gate electrode. A pulsed signal with a frequency of 5 Hz, a 50% duty cycle, and a $V_G$ from −0.2 V to 0.6 V (with a $V_D$ of 0.1 V) was applied for 50 000 pulses over 10 000 s. After every 2500 pulses, a transfer characteristic measurement was conducted. The initial 2500 cycles served to stabilize the BBL polymer system, after which the transfer characteristic was recorded as transfer-0 and the corresponding extracted parameters were defined as $I_{on\text{-}0}$, $g_{m\text{-}0}$, and $I_{off\text{-}0}$. For subsequent cycles, the extracted values were labeled as $I_{on\text{-}x}$, $g_{m\text{-}x}$, and $I_{off\text{-}x}$.

### Film thickness characterization

The film thickness was characterized by atomic force microscopy (AFM). AFM characterization was performed in tapping mode under ambient conditions.

### EIS measurements

EIS measurements were conducted using a Gamry Reference 620. Characterization was performed through the two-electrode measurement, where the source and drain electrodes of the vOECT were shorted to serve as the working electrode, while an Ag/AgCl electrode was used as both the counter and reference electrodes. The DC bias applied to the working electrodes was −0.6 V and the AC bias was 10 mV.

## Data availability

The data that support the findings of this study are available from the corresponding author upon reasonable request.

## Conflicts of interest

There are no conflicts to declare.

## Acknowledgements

This work was financially supported by the National Key R&D Program of China (2022YFE0134800), the National Natural Science Foundation of China (No. 62273073), the National Key R&D Program of China (2024YFB4611600 and 2023YFC2411800), the Aeronautical Science Foundation of China (20230024080002), the Sichuan Science and Technology Program (No. 2023ZYD0161), Natural Science Foundation of Sichuan (2025ZNSFSC0515), the Chengdu Science Technology Bureau (2023-YF06-00028-HZ), and the Fundamental Research Funds for the Central Universities (ZYGX2024XJ029). This work was also sponsored by the China

Published on 07 March 2025. Downloaded on 3/15/2026 4:49:12 AM.

Postdoctoral Science Foundation (GZB20230116 and 2024M750343).

## References

1 B. D. Paulsen, K. Tybrandt, E. Stavrinidou and J. Rivnay, *Nat. Mater.*, 2020, **19**, 13–26.
2 J. Rivnay, S. Inal, A. Salleo, R. M. Owens, M. Berggren and G. G. Malliaras, *Nat. Rev. Mater.*, 2018, **3**, 17086.
3 F. Torricelli, D. Z. Adrahtas, Z. Bao, M. Berggren, F. Biscarini, A. Bonfiglio, C. A. Bortolotti, C. D. Frisbie, E. Macchia, G. G. Malliaras, I. McCulloch, M. Moser, T.-Q. Nguyen, R. M. Owens, A. Salleo, A. Spanu and L. Torsi, *Nat. Rev. Methods Primers*, 2021, **1**, 66.
4 X. Ji, X. Lin and J. Rivnay, *Nat. Commun.*, 2023, **14**, 1665.
5 H. Liu, A. Yang, J. Song, N. Wang, P. Lam, Y. Li, H. K.-w. Law and F. Yan, *Sci. Adv.*, 2021, **7**, eabg8387.
6 S. Inal, G. G. Malliaras and J. Rivnay, *Nat. Commun.*, 2017, **8**, 1767.
7 P. Andersson Ersman, R. Lassnig, J. Strandberg, D. Tu, V. Keshmiri, R. Forchheimer, S. Fabiano, G. Gustafsson and M. Berggren, *Nat. Commun.*, 2019, **10**, 5053.
8 J. Kim, R. M. Pankow, Y. Cho, I. D. Duplessis, F. Qin, D. Meli, R. Daso, D. Zheng, W. Huang, J. Rivnay, T. J. Marks and A. Facchetti, *Nat. Electron.*, 2024, **7**, 234–243.
9 R. B. Rashid, X. Ji and J. Rivnay, *Biosens. Bioelectron.*, 2021, **190**, 113461.
10 P. C. Harikesh, C.-Y. Yang, D. Tu, J. Y. Gerasimov, A. M. Dar, A. Armada-Moreira, M. Massetti, R. Kroon, D. Bliman, R. Olsson, E. Stavrinidou, M. Berggren and S. Fabiano, *Nat. Commun.*, 2022, **13**, 901.
11 S. Wang, X. Chen, C. Zhao, Y. Kong, B. Lin, Y. Wu, Z. Bi, Z. Xuan, T. Li, Y. Li, W. Zhang, E. Ma, Z. Wang and W. Ma, *Nat. Electron.*, 2023, **6**, 281–291.
12 S. T. Keene, C. Lubrano, S. Kazemzadeh, A. Melianas, Y. Tuchman, G. Polino, P. Scognamiglio, L. Cinà, A. Salleo, Y. van de Burgt and F. Santoro, *Nat. Mater.*, 2020, **19**, 969–973.
13 E. R. W. van Doremaele, X. Ji, J. Rivnay and Y. van de Burgt, *Nat. Electron.*, 2023, **6**, 765–770.
14 Y. van de Burgt, E. Lubberman, E. J. Fuller, S. T. Keene, G. C. Faria, S. Agarwal, M. J. Marinella, A. A. Talin and A. Salleo, *Nat. Mater.*, 2017, **16**, 414–418.
15 Y. Choi, S. Oh, C. Qian, J.-H. Park and J. H. Cho, *Nat. Commun.*, 2020, **11**, 4595.
16 L. Q. Flagg, C. G. Bischak, J. W. Onorato, R. B. Rashid, C. K. Luscombe and D. S. Ginger, *J. Am. Chem. Soc.*, 2019, **141**, 4345–4354.
17 P. Li and T. Lei, *J. Polym. Sci.*, 2022, **60**, 377–392.
18 Y. Wang, S. Wustoni, J. Surgailis, Y. Zhong, A. Koklu and S. Inal, *Nat. Rev. Mater.*, 2024, **9**, 249–265.
19 A. Saleh, A. Koklu, I. Uguz, A.-M. Pappa and S. Inal, *Nat. Rev. Bioeng.*, 2024, **2**, 559–574.
20 P. Romele, M. Ghittorelli, Z. M. Kovács-Vajna and F. Torricelli, *Nat. Commun.*, 2019, **10**, 3044.
21 S. Yu and E. L. Ratcliff, *ACS Appl. Mater. Interfaces*, 2021, **13**, 50176–50186.
22 W. Huang, J. Chen, Y. Yao, D. Zheng, X. Ji, L.-W. Feng, D. Moore, N. R. Glavin, M. Xie, Y. Chen, R. M. Pankow, A. Surendran, Z. Wang, Y. Xia, L. Bai, J. Rivnay, J. Ping, X. Guo, Y. Cheng, T. J. Marks and A. Facchetti, *Nature*, 2023, **613**, 496–502.
23 J. Rivnay, P. Leleux, M. Ferro, M. Sessolo, A. Williamson, D. A. Koutsouras, D. Khodagholy, M. Ramuz, X. Strakosas, R. M. Owens, C. Benar, J.-M. Badier, C. Bernard and G. G. Malliaras, *Sci. Adv.*, 2015, **1**, e1400251.
24 J. Brodský, I. Gablech, L. Migliaccio, M. Havlíček, M. J. Donahue and E. D. Głowacki, *ACS Appl. Mater. Interfaces*, 2023, **15**, 27002–27009.
25 M. Xie, Y. Lai, M. Li, D. Zhao, C. Huang, L. Bai, Y. Cheng, J. Chen, L.-W. Feng and W. Huang, *J. Mater. Chem. A*, 2024, **12**, 15753–15761.
26 L. Gao, Q. Zhang, Y. Lai, M. Xie, C. Liu, D. Zhang, Y. Peng, L. Bai, M. Wu, L.-W. Feng, W. Huang, J. Yu and X. Yu, *Nano Energy*, 2024, **129**, 110062.
27 X. Zhang, W. Deng, R. Jia, X. Zhang and J. Jie, *Small*, 2019, **15**, 1900332.
28 M. Höppner, D. Kneppe, H. Kleemann and K. Leo, *Org. Electron.*, 2020, **76**, 105357.
29 Y. Lai, J. Cheng, M. Xie, J. Chen, G. Zhu, W. Huang and L.-W. Feng, *Angew. Chem., Int. Ed.*, 2024, **63**, e202401773.
30 A. Enrico, S. Buchmann, F. De Ferrari, Y. Lin, Y. Wang, W. Yue, G. Mårtensson, G. Stemme, M. M. Hamedi, F. Niklaus, A. Herland and E. Zeglio, *Adv. Sci.*, 2024, **11**, 2307042.
31 J. Park, X. Zhang, M.-H. Bae, G.-T. Park and J.-H. Bae, *Jpn. J. Appl. Phys.*, 2013, **52**, 111602.
32 A. G. Polyravas, V. F. Curto, N. Schaefer, A. B. Calia, A. Guimera-Brunet, J. A. Garrido and G. G. Malliaras, *Flexible Printed Electron.*, 2019, **4**, 044003.
33 D. A. Bernards and G. G. Malliaras, *Adv. Funct. Mater.*, 2007, **17**, 3538–3544.
34 C. Chen, Z. Chen, K. Xu, J. Zheng, H. Ou, Z. Wang, H. Chen, X. Liu, Q. Wu, P. K. L. Chan and C. Liu, *IEEE Electron Device Lett.*, 2019, **40**, 897–900.
35 V. Kaphle, P. R. Paudel, D. Dahal, R. K. Radha Krishnan and B. Lüssem, *Nat. Commun.*, 2020, **11**, 2515.
36 J. T. Friedlein, M. J. Donahue, S. E. Shaheen, G. G. Malliaras and R. R. McLeod, *Adv. Mater.*, 2016, **28**, 8398–8404.
37 G. C. Faria, D. T. Duong and A. Salleo, *Org. Electron.*, 2017, **45**, 215–221.
38 J. T. Friedlein, R. R. McLeod and J. Rivnay, *Org. Electron.*, 2018, **63**, 398–414.
39 D. Fazzi and F. Negri, *Adv. Electron. Mater.*, 2021, **7**, 2000786.

 This journal is © The Royal Society of Chemistry 2025

40 J. Chen, W. Huang, D. Zheng, Z. Xie, X. Zhuang, D. Zhao, Y. Chen, N. Su, H. Chen, R. M. Pankow, Z. Gao, J. Yu, X. Guo, Y. Cheng, J. Strzalka, X. Yu, T. J. Marks and A. Facchetti, *Nat. Mater.*, 2022, **21**, 564–571.
41 Y.-Q. Zheng, Y. Liu, D. Zhong, S. Nikzad, S. Liu, Z. Yu, D. Liu, H.-C. Wu, C. Zhu, J. Li, H. Tran, J. B. H. Tok and Z. Bao, *Science*, 2021, **373**, 88–94.
42 Z. Wang, X. Zhuang, Y. Chen, B. Wang, J. Yu, W. Huang, T. J. Marks and A. Facchetti, *Chem. Mater.*, 2019, **31**, 7608–7617.

Published on 07 March 2025. Downloaded on 3/15/2026 4:49:12 AM.